

LivePortrait: Efficient Portrait Animation with Stitching and Retargeting Control

Jianzhu Guo¹ Dingyun Zhang^{1,2} Xiaoqiang Liu¹ Zhizhou Zhong^{1,3} Yuan Zhang¹ Pengfei Wan¹ Di Zhang¹
¹Kuaishou Technology ²University of Science and Technology of China ³Fudan University

<https://liveportrait.github.io>

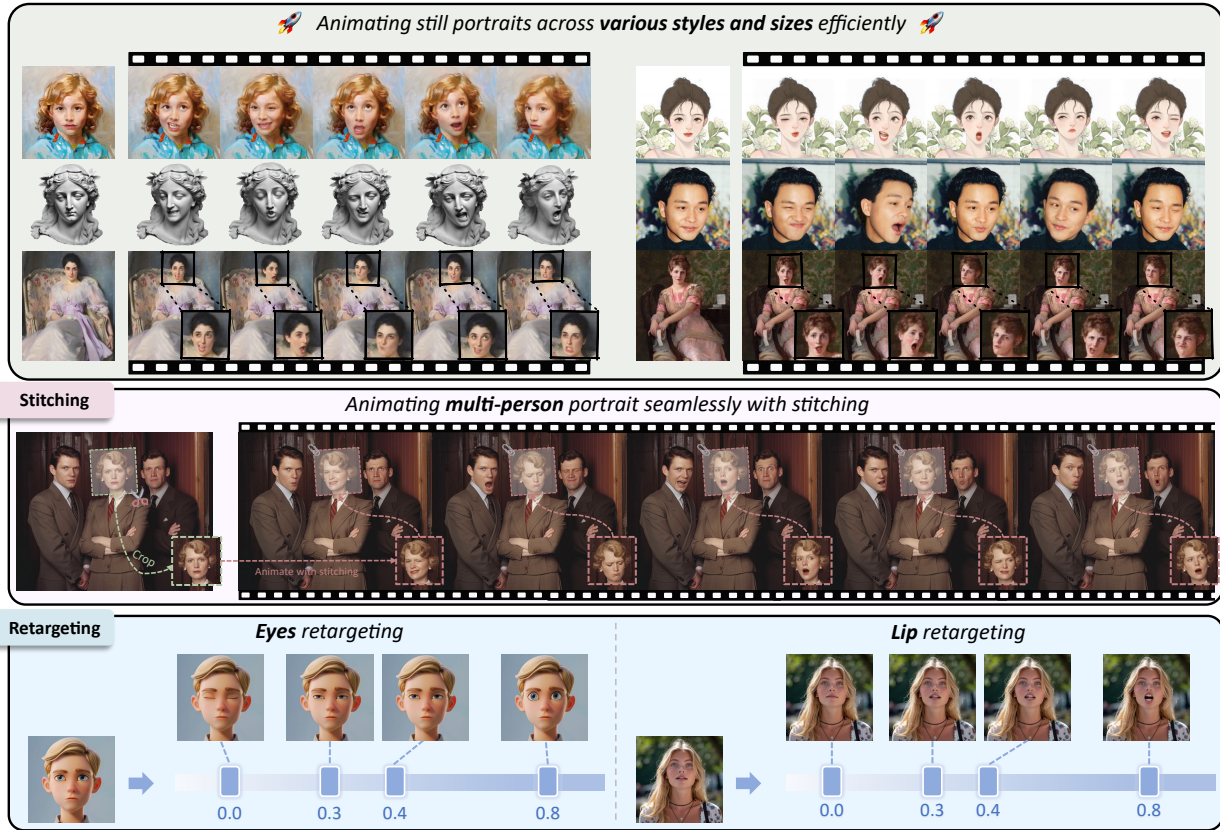


Figure 1. **Qualitative portrait animation results from our model.** Given a static portrait image as input, our model can vividly animate it, ensuring seamless stitching and offering precise control over eyes and lip movements.

Abstract

Portrait animation aims to synthesize a lifelike video from a single source image, using it as an appearance reference, with motion (i.e., facial expressions and head pose) derived from a driving video, audio, text, or generation. Instead of following mainstream diffusion-based methods, we explore and extend the potential of the implicit-keypoint-based framework, which effectively balances computational efficiency and controllability. Building upon this, we develop a video-driven portrait animation framework named **LivePortrait** with a focus on better generalization, controllability, and efficiency for practical usage. To enhance the generation quality and generalization ability, we scale up the train-

ing data to about 69 million high-quality frames, adopt a mixed image-video training strategy, upgrade the network architecture, and design better motion transformation and optimization objectives. Additionally, we discover that compact implicit keypoints can effectively represent a kind of blendshapes and meticulously propose a stitching and two retargeting modules, which utilize a small MLP with negligible computational overhead, to enhance the controllability. Experimental results demonstrate the efficacy of our framework even compared to diffusion-based methods. The generation speed remarkably reaches 12.8ms on an RTX 4090 GPU with PyTorch. The inference code and models are available at <https://github.com/KwaiVGI/LivePortrait>.

1. Introduction

Nowadays, people frequently use smartphones or other recording devices to capture static portraits to record their precious moments. The Live Photos¹ feature on iPhone can bring static portraits to life by recording the moments 1.5 seconds before and after a picture is taken, which is likely achieved through a form of video recording. However, based on recent advances like GANs [1] and Diffusions [2–4], various portrait animation methods [5–13] have made it possible to animate a static portrait into dynamic ones, without relying on specific recording devices.

In this paper, we aim to animate a static portrait image, making it realistic and expressive, while also pursuing high inference efficiency and precise controllability. Although diffusion-based portrait animation methods [12–14] have achieved impressive results in terms of quality, they are usually computationally expensive and lack the precise controllability, *e.g.*, stitching control². Instead, we extensively explore implicit-keypoint-based video-driven frameworks [5, 11], and extend their potential to effectively balance the generalization ability, computational efficiency, and controllability.

Specifically, we first enhance a powerful implicit-keypoint-based method [5], by scaling up the training data to about 69 million high-quality portrait images, introducing a mixed image-video training strategy, upgrading the network architecture, using the scalable motion transformation, designing the landmark-guided implicit keypoints optimization and several cascaded loss terms. Additionally, we discover that compact implicit keypoints can effectively represent a kind of implicit blendshapes, and meticulously design a stitching module and two retargeting modules, which utilize a small MLP and add negligible computational overhead, to enhance the controllability, such as stitching control. Our core contributions can be summarized as follows: (i) developing a solid implicit-keypoint-based video-driven portrait animation framework that significantly enhances the generation quality and generalization ability, and (ii) designing an advanced stitching module and two retargeting modules for better controllability, with negligible computational overhead. Extensive experimental results demonstrate the efficacy of our framework, even compared to heavy diffusion-based methods. Besides, our model can generate a portrait animation in 12.8ms on an RTX 4090 GPU using PyTorch for inference.

2. Related Work

Recent video-driven portrait animation methods can be divided into non-diffusion-based and diffusion-based methods, as summarized in Tab. 1.

¹<https://support.apple.com/en-sg/104966>

²<https://www.d-id.com/liveportrait-4>

2.1. Non-diffusion-based Portrait Animation

For non-diffusion-based models, the implicit-keypoints-based methods employed implicit keypoints as the intermediate motion representation, and warped the source portrait with the driving image by the optical flow. FOMM [11] performed first-order Taylor expansion near each keypoint and approximated the motion in the neighborhood of each keypoint using local affine transformations. MRAA [15] represented articulated motion with PCA-based motion estimation. Face vid2vid [5] extended FOMM by introducing 3D implicit keypoints representation and achieved free-view portrait animation. IWA [10] improved the warping mechanism based on cross-modal attention, which can be extended to using multiple source images. To estimate the optical flow more flexibly and work better for large-scale motions, TPSM [7] used nonlinear thin-plate spline transformation for representing more complex motions. Simultaneously, DaGAN [6] leveraged the dense depth maps to estimate implicit keypoints that capture the critical driving movements. MCNet [8] designed an identity representation conditioned memory compensation network to tackle the ambiguous generation caused by the complex driving motions.

Several works [18–20] employed predefined motion representations, such as 3DMM blendshapes [21]. Another line of works [22, 23] proposed to learn the latent expression representation from scratch. MegaPortrait [22] used the high-resolution images beyond the medium-resolution training images to upgrade animated resolution to megapixel. EMO-Portraits [23] employed an expression-riched training video dataset and the expression-enhanced loss to express the intense motions.

2.2. Diffusion-based Portrait Animation

Diffusion models [2–4] synthesized the desired data samples from Gaussian noise via removing noises iteratively. [2] proposed the Latent Diffusion Models (LDMs) and transferred the training and inference processes to a compressed latent space for efficient computing. LDMs have been broadly applied to many concurrent works in full-body dance generation [24–28], audio-driven portrait animation [12, 29–34], and video-driven portrait animation [9, 12, 13, 16].

FADM [9] was the first diffusion-based portrait animation method. It obtained the coarsely animated result via the pretrained implicit-keypoints-based model and then got the final animation under the guidance of the 3DMMs with the diffusion model. Face Adapter [16] used an identity adapter to enhance the identity preservation of the source portrait and a spatial condition generator to generate the explicit spatial condition, *i.e.*, keypoints and foreground masks, as the intermediate motion representation. Several works [12, 13, 17] employed the mutual self-attention and plugged temporal attention architecture similar to AnimateAnyone [24] to achieve better image quality and appearance preserva-

Method	Framework	Intermediate motion representation	Generation ability	Inference efficiency	Controllability		
					Stitching	Eyes retargeting	Lip retargeting
FOMM [11] MRAA [15] Face Vid2vid [5] IWA [10] TPSM [7] DaGAN [6] MCNet [8]	Non-diffusion	Implicit keypoints	★★★	😊	✗	✗	✗
FADM [9]	Diffusion	Implicit keypoints + 3DMMs	★★★	😞	✗	✗	✗
Face Adapter [16] AniPortrait [12]	Diffusion	Explicit keypoints or masks	★★★★	😞	✗	✗	✗
X-Portrait [13]	Diffusion	Only original driving images	★★★★★	😞	✗	✗	✗
MegActor [17]	Diffusion	Only original driving images	★★★★	😞	✗	✗	✗
Ours	Non-diffusion	Implicit keypoints	★★★★	😊	✓	✓	✓

Table 1. Summary of the video-driven portrait animation methods.

tion. AniPortrait [12] used the explicit spatial condition, *i.e.*, keypoints, as the intermediate motion representation. X-Portrait [13] proposed to animate the portraits directly with the original driving video instead of using the intermediate motion representations. It employed the implicit-keypoint-based method [5] for cross-identity training to achieve this. MegActor [17] also animated the source portrait with the original driving video. It employed the existing face-swapping and stylization framework to get the cross-identity training pairs and encoded the background appearance to improve the animation stability.

3. Methodology

This section details our method. We begin with a brief review of the video-based portrait animation framework face vid2vid [5] and introduce our significant enhancements aimed at enhancing the generalization ability and expressiveness of animation. Then, we present our meticulously designed stitching and retargeting modules which provide desired controllability with negligible computational overhead. Finally, we detail the inference pipeline.

3.1. Preliminary of Face Vid2vid

Face vid2vid [5] is a seminal framework for animating a still portrait, using the motion features extracted from the driving video sequence. The original framework consists of an appearance feature extractor \mathcal{F} , a canonical implicit keypoint detector \mathcal{L} , a head pose estimation network \mathcal{H} , an expression deformation estimation network Δ , a warping field estimator \mathcal{W} , and a generator \mathcal{G} . \mathcal{F} maps the source image s to a 3D appearance feature volume f_s . The source 3D keypoints x_s and the driving 3D keypoints x_d are transformed as follows:

$$\begin{cases} x_s = x_{c,s}R_s + \delta_s + t_s, \\ x_d = x_{c,s}R_d + \delta_d + t_d, \end{cases} \quad (1)$$

where x_s and x_d are the source and driving 3D implicit keypoints, respectively, and $x_{c,s} \in \mathbb{R}^{K \times 3}$ represents the canonical keypoints of the source image. The source and driving poses are R_s and $R_d \in \mathbb{R}^{3 \times 3}$, the expression deformations are δ_s and $\delta_d \in \mathbb{R}^{K \times 3}$, and the translations are t_s and $t_d \in \mathbb{R}^3$. Next, \mathcal{W} generates a warping field using the implicit keypoint representations x_s and x_d , and employs this flow field to warp the source feature volume f_s . Subsequently, the warped features pass through a decoder generator \mathcal{G} , translating them into image space and resulting in a target image.

3.2. Stage I: Base Model Training

We choose face vid2vid [5] as our base model and introduce a series of significant enhancements. These include high-quality data curation, a mixed image and video training strategy, an upgraded network architecture, scalable motion transformation, landmark-guided implicit keypoints optimization, and cascaded loss terms. These advancements significantly enhance the expressiveness of the animation and the generalization ability of the model. The pipeline of the first training stage is shown in Fig. 2.

High quality data curation. We leverage public video datasets such as Voxceleb [35], MEAD [36], and RAVDESS [37], as well as the styled image dataset AAHQ [38]. Additionally, we collect a large corpus of 4K-resolution portrait videos with various poses and expressions, 200 hours of talking head videos, and utilize the private LightStage [39, 40] dataset, along with several styled portrait videos and images. We split long videos into clips of less than 30 seconds and ensure each clip contains only one person using face tracking and recognition. To maintain the quality of the training data, we use KVQ [41] to filter out low-quality video clips. Finally, our training data consists of

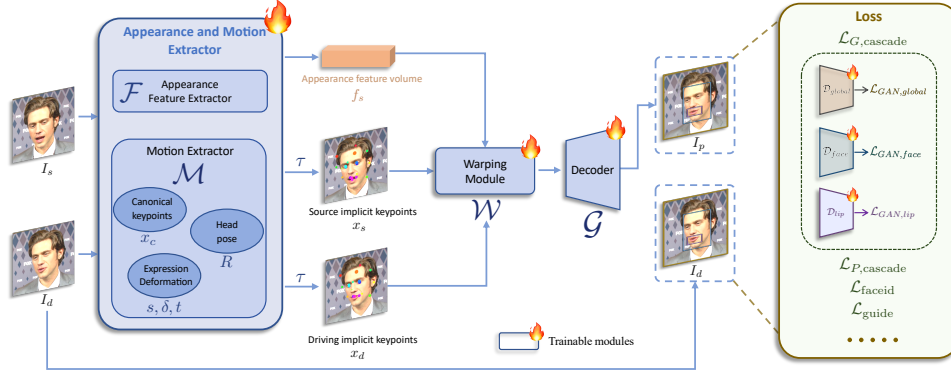


Figure 2. **Pipeline of the first stage: base model training.** The appearance and motion extractors \mathcal{F} and \mathcal{M} , the warping module \mathcal{W} , and the decoder \mathcal{G} are optimized. In this stage, models are trained from scratch. Please refer to Sec. 3.2 for details.

69M video frames (92M before filtering) from about 18.9K identities and 60K static styled portraits.

Mixed image and video training. The model trained only on realistic portrait videos performs well on human portraits but generalizes poorly to styled portraits, *e.g.*, anime. Styled portrait videos are scarce, we collect only about 1.3K clips from fewer than 100 identities. In contrast, high-quality styled portrait images are more abundant; we gathered approximately 60K images, each representing a unique identity, offering diverse identity information. To leverage both data types, we treat single images as one-frame video clips and train the model on both images and videos. This mixed training improves the model’s generalization ability.

Upgraded network architecture. We unify the original canonical implicit keypoint detector \mathcal{L} , head pose estimation network \mathcal{H} , and expression deformation estimation network Δ into a single model \mathcal{M} , with ConvNeXt-V2-Tiny [42] as the backbone, which directly predicts the canonical keypoints, head pose and expression deformation of the input image. Additionally, we follow [43] to use SPADE decoder [44] as the generator \mathcal{G} , which is more powerful than the original decoder in face vid2vid [5]. The warped feature volume f_s is delicately fed into the SPADE decoder, where each channel of the feature volume serves as a semantic map to generate the animated image. For efficiency, we insert a PixelShuffle [45] layer as the final layer of \mathcal{G} to upsample the resolution from 256×256 to 512×512 .

Scalable motion transformation. The original implicit keypoint transformation in Eqn. 1 ignores the scale factor, which tends to incorporate scaling into the expression deformation and increases the training difficulty. To address this issue, we introduce a scale factor to the motion transformation, and the updated transformation τ is formulated as:

$$\begin{cases} x_s = s_s \cdot (x_{c,s}R_s + \delta_s) + t_s, \\ x_d = s_d \cdot (x_{c,s}R_d + \delta_d) + t_d, \end{cases} \quad (2)$$

where s_s and s_d are the scale factors of the source and driving input, respectively. Note that the transformation differs from the scale orthographic projection, which is formulated as $x = s \cdot ((x_c + \delta)R) + t$. We find that the scale orthographic projection leads to overly flexible learned expressions δ , causing texture flickering when driving across different identities. Therefore, this transformation can be seen as a tradeoff between flexibility and drivability.

Landmark-guided implicit keypoints optimization. The original face vid2vid [5, 43] seems to lack the ability to vividly drive facial expressions, such as winking and eye movements. In particular, the eye gazes of generated portraits are bound to the head pose and remain parallel to it, a limitation we also observed in our reproduction experiments. We attribute these limitations to the difficulty of learning subtle facial expressions, like eye movements, in an unsupervised manner. To address this, we introduce 2D landmarks that capture micro-expressions, using them as guidance to optimize the learning of implicit points. The landmark-guided loss $\mathcal{L}_{\text{guide}}$ is formulated as follows:

$$\mathcal{L}_{\text{guide}} = \frac{1}{2N} \sum_{i=1}^N (\text{Wing}(l_i, x_{s,i,:2}) + \text{Wing}(l_i, x_{d,i,:2})), \quad (3)$$

where N is the number of selected landmarks, l_i is the i -th landmark, $x_{s,i,:2}$ and $x_{d,i,:2}$ represent the first two dimensions of the corresponding implicit keypoints respectively, and Wing loss is adopted following [46]. In our experiments, N is set to 10, with the selected landmarks taken from the eyes and lip.

Cascaded loss terms. We follow face vid2vid [5] to use implicit keypoints equivariance loss \mathcal{L}_E , keypoint prior loss

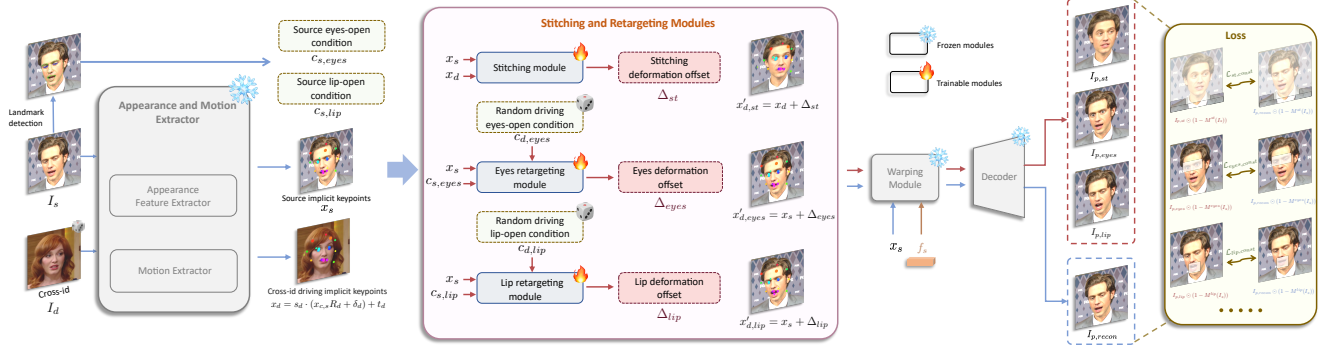


Figure 3. Pipeline of the second stage: stitching and retargeting modules training. After training the base model in the first stage, we freeze the appearance and motion extractor, warping module and decoder. Only the stitching module and the retargeting modules are optimized in the second stage. Please refer to Sec. 3.3 for details.

\mathcal{L}_L , head pose loss \mathcal{L}_H , and deformation prior loss \mathcal{L}_Δ . To further improve the texture quality, we apply perceptual and GAN losses on the global region of the input image, and local regions of face and lip, denoted as a cascaded perceptual loss $\mathcal{L}_{P,cascade}$ and a cascaded GAN loss $\mathcal{L}_{G,cascade}$. $\mathcal{L}_{G,cascade}$ consists of $\mathcal{L}_{GAN,global}$, $\mathcal{L}_{GAN,face}$, and $\mathcal{L}_{GAN,lip}$, which depend on the corresponding discriminators \mathcal{D}_{global} , \mathcal{D}_{face} , and \mathcal{D}_{lip} training from scratch. The face and lip regions are defined by 2D semantic landmarks. We also adopt a face-id [47] loss \mathcal{L}_{faceid} to preserve the identity of the source image. The overall training objective of the first stage is formulated as:

$$\begin{aligned} \mathcal{L}_{base} = & \mathcal{L}_E + \mathcal{L}_L + \mathcal{L}_H + \mathcal{L}_\Delta + \\ & \mathcal{L}_{P,cascade} + \mathcal{L}_{G,cascade} + \mathcal{L}_{faceid} + \mathcal{L}_{guide}. \end{aligned} \quad (4)$$

During the first stage, the model is fully trained from scratch.

3.3. Stage II: Stitching and Retargeting

We suppose the compact implicit keypoints can serve as a kind of implicit blendshapes. Unlike pose, we cannot explicitly control the expressions, but rather need a combination of these implicit blendshapes to achieve the desired effects. Surprisingly, we discover that such a combination can be well learned using only a small MLP network, with negligible computational overhead. Considering practical requirements, we design a stitching module, an eyes retargeting module, and a lip retargeting module. The stitching module pastes the animated portrait back into the original image space without pixel misalignment, such as in the shoulder region. This enables the handling of much larger image sizes and the animation of multiple faces simultaneously. The eyes retargeting module is designed to address the issue of incomplete eye closure during cross-id reenactment, especially when a person with small eyes drives a person with larger eyes. The lip retargeting module is designed similarly to the eye retargeting module, and can also normalize the input by ensuring that the lips are in a closed state, which facilitates

better animation driving. The pipeline of the second training stage is shown in Fig. 3.

Stitching module. During training, the stitching module \mathcal{S} receives the source and driving implicit keypoints x_s and x_d as input, and estimates a deformation offset $\Delta_{st} \in \mathbb{R}^{K \times 3}$ of the driving keypoints. Following Eqn. 2, the source implicit keypoints are calculated as $x_s = s_s \cdot (x_{c,s}R_s + \delta_s) + t_s$, and the driving implicit keypoints x_d are calculated using another person’s motions as $x_d = s_d \cdot (x_{c,s}R_d + \delta_d) + t_d$. Note that the transformation of x_d differs from the first training stage, as we deliberately use cross-id rather than same-id motion to increase training difficulty, aiming for better generalization in stitching. Then, $\Delta_{st} = \mathcal{S}(x_s, x_d)$, the driving keypoints are updated as $x'_{d,st} = x_d + \Delta_{st}$, and the prediction image $I_{p,st} = \mathcal{D}(\mathcal{W}(f_s; x_s, x'_{d,st}))$. We denote the self-reconstruction image as $I_{p,recon} = \mathcal{D}(\mathcal{W}(f_s; x_s, x_s))$. Finally, the stitching objective \mathcal{L}_{st} is formulated as:

$$\mathcal{L}_{st} = \underbrace{\| (I_{p,st} - I_{p,recon}) \odot (1 - M^{st}(I_s)) \|_1}_{\mathcal{L}_{st,const}} + w_{reg}^{st} \|\Delta_{st}\|_1, \quad (5)$$

where $\mathcal{L}_{st,const}$ is the consistency pixel loss between the shoulder region of the prediction and the self-reconstruction image, M^{st} is a mask operator that masks out the non-shoulder region from the source image I_s , which is visualized in Fig. 3. $\|\Delta_{st}\|_1$ is the L_1 norm regularization of the stitching deformation offset, and w_{reg}^{st} is a hyperparameter.

Eyes and lip retargeting modules. The eyes retargeting module \mathcal{R}_{eyes} receives the source implicit keypoints x_s , the source eyes-open condition tuple $c_{s,eyes}$ and a random driving eyes-open scalar $c_{d,eyes} \in [0, 0.8]$ as input, estimating a deformation offset $\Delta_{eyes} \in \mathbb{R}^{K \times 3}$ for the driving keypoints: $\Delta_{eyes} = \mathcal{R}_{eyes}(x_s; c_{s,eyes}, c_{d,eyes})$. The eyes-open condition denotes the ratio of eye-opening: the larger the value, the more open the eyes. Similarly, the lip retargeting

module \mathcal{R}_{lip} also receives the source implicit keypoints x_s and the source lip-open condition scalar $c_{s,lip}$ and a random driving lip-open scalar $c_{d,lip}$ as input, estimating a deformation offset $\Delta_{lip} \in \mathbb{R}^{K \times 3}$ for the driving keypoints: $\Delta_{lip} = \mathcal{R}_{lip}(x_s; c_{s,lip}, c_{d,lip})$. Then, the driving keypoints are updated as $x'_{d,eyes} = x_s + \Delta_{eyes}$ and $x'_{d,lip} = x_s + \Delta_{lip}$, and the prediction images are $I_{p,eyes} = \mathcal{D}(\mathcal{W}(f_s; x_s, x'_{d,eyes}))$ and $I_{p,lip} = \mathcal{D}(\mathcal{W}(f_s; x_s, x'_{d,lip}))$. Finally, the training objectives for the eyes and lip retargeting modules are formulated as follows:

$$\begin{aligned} \mathcal{L}_{eyes} &= \underbrace{\| (I_{p,eyes} - I_{p,recon}) \odot (1 - M^{eyes}(I_s)) \|_1}_{\mathcal{L}_{eyes, const}} + \\ &\quad w_{cond}^{eyes} \| c_{s,eyes}^p - c_{d,eyes} \|_1 + w_{reg}^{eyes} \| \Delta_{eyes} \|_1, \\ \mathcal{L}_{lip} &= \underbrace{\| (I_{p,lip} - I_{p,recon}) \odot (1 - M^{lip}(I_s)) \|_1}_{\mathcal{L}_{lip, const}} + \\ &\quad w_{cond}^{lip} \| c_{s,lip}^p - c_{d,lip} \|_1 + w_{reg}^{lip} \| \Delta_{lip} \|_1, \end{aligned} \quad (6)$$

where M^{eyes} and M^{lip} are mask operators that mask out the eyes and lip regions from the source image I_s respectively, $c_{s,eyes}^p$ and $c_{s,lip}^p$ are the condition tuples from $I_{p,eyes}$, $I_{p,lip}$ respectively, and w_{cond}^{eyes} , w_{reg}^{eyes} , w_{cond}^{lip} , w_{reg}^{lip} are hyperparameters.

3.4. Inference

In the inference phase, we first extract the feature volume $f_s = \mathcal{F}(I_s)$, the canonical keypoints $x_{c,s} = \mathcal{M}(I_s)$ from the source image I_s . Given a driving video sequence $\{I_{d,i} | i = 0, \dots, N-1\}$, we extract motions from each frame $s_{d,i}, \delta_{d,i}, t_{d,i}, R_{d,i} = \mathcal{M}(I_{d,i})$ and conditions $c_{d,eyes,i}$ and $c_{d,lip,i}$. The source and driving implicit keypoints are next transformed as follows:

$$\begin{cases} x_s &= s_s \cdot (x_{c,s} R_s + \delta_s) + t_s, \\ x_{d,i} &= s_s \cdot \frac{s_{d,i}}{s_{d,0}} \cdot (x_{c,s} (R_{d,i} R_{d,0}^{-1} R_s) + \\ &\quad (\delta_s + \delta_{d,i} - \delta_{d,0})) + (t_s + t_{d,i} - t_{d,0}). \end{cases} \quad (7)$$

Then, the inference procedure could be described as in Algorithm 1, where α_{st} , α_{eyes} and α_{lip} are indicator variables that can take values of either 0 or 1. The final prediction image $I_{p,i}$ is generated by the warping network \mathcal{W} and the decoder \mathcal{D} . Note that the deformation offsets of eyes and lip are decoupled from each other, allowing them to be linearly added to the driving keypoints.

4. Experiments

We first give an overview of the implementation details, baselines, and benchmarks used in the experiments. Then, we present the experimental results on self-reenactment and cross-reenactment, followed by an ablation study to validate the effectiveness of the proposed stitching and retargeting modules.

Algorithm 1 Illustration of the inference procedure

Input: $f_s; x_s, x_{d,i}; \alpha_{eyes}, \alpha_{lip}, \alpha_{st}; c_{s,eyes}, c_{d,eyes,i}, c_{s,lip}, c_{d,lip,i}$
Output: $I_{p,i}$

- 1: **if** $\alpha_{st} = 0$ and $\alpha_{eyes} = 0$ and $\alpha_{lip} = 0$ **then**
- 2: \triangleright *without stitching or retargeting* ◁
- 3: $x'_{d,i} \leftarrow x_{d,i}$
- 4: **else if** $\alpha_{st} = 1$ and $\alpha_{eyes} = 0$ and $\alpha_{lip} = 0$ **then**
- 5: \triangleright *with stitching and without retargeting* ◁
- 6: $\Delta_{st,i} = \mathcal{S}(x_s, x_{d,i})$
- 7: $x'_{d,i} \leftarrow x_{d,i} + \Delta_{st,i}$
- 8: **else if** $\alpha_{eyes} = 1$ or $\alpha_{lip} = 1$ **then**
- 9: \triangleright *with eyes or lip retargeting* ◁
- 10: $\Delta_{eyes,i} = \mathcal{R}_{eyes}(x_s; c_{s,eyes}, c_{d,eyes,i})$
- 11: $\Delta_{lip,i} = \mathcal{R}_{lip}(x_s; c_{s,lip}, c_{d,lip,i})$
- 12: $x'_{d,i} \leftarrow x_s + \alpha_{eyes} \Delta_{eyes,i} + \alpha_{lip} \Delta_{lip,i}$
- 13: **if** $\alpha_{st} = 1$ **then**
- 14: $\Delta_{st,i} = \mathcal{S}(x_s, x'_{d,i})$
- 15: $x'_{d,i} \leftarrow x'_{d,i} + \Delta_{st,i}$
- 16: **end if**
- 17: **end if**
- 18: $I_{p,i} \leftarrow \mathcal{D}(\mathcal{W}(f_s; x_s, x'_{d,i}))$

Implementation Details. In the first training stage, our models are trained from scratch using 8 NVIDIA A100 GPUs for approximately 10 days. During the second training stage, we only train the stitching and retargeting modules while keeping other parameters frozen, which takes approximately 2 days. The input images are aligned and cropped to a resolution of 256×256 , with a batch size set to 104. The output resolution is 512×512 . The Adam optimizer is employed with a learning rate of 2×10^{-4} , $\beta_1 = 0.5$, and $\beta_2 = 0.999$. The stitching module consists of a four-layer MLP with layer sizes of [126, 128, 128, 64, 65]. The eyes retargeting module consists of a six-layer MLP with layer sizes of [66, 256, 256, 128, 128, 64, 63]. The lip retargeting module consists of a four-layer MLP with layer sizes of [65, 128, 128, 64, 63]. The computation budget of the stitching and retargeting modules is negligible.

Baselines. We compare our model with several non-diffusion-based methods, including FOMM [11], Face Vid2vid [5], DaGAN [6], MCNet [8], and TPSM [7], as well as diffusion-based models such as FADM [9] and Ani-Portrait [12]. For face vid2vid [5], we employ the implementation from [43], while for the other methods, we use the official implementations.

Benchmarks. To measure the generalization quality and motion accuracy of portrait animation results, we adopt Peak Signal-to-Noise Ratio (PSNR), Structural Similarity Index (SSIM) [48], Learned Perceptual Image Patch Similarity (LPIPS) [49], \mathcal{L}_1 distance, FID [50], Average Expression

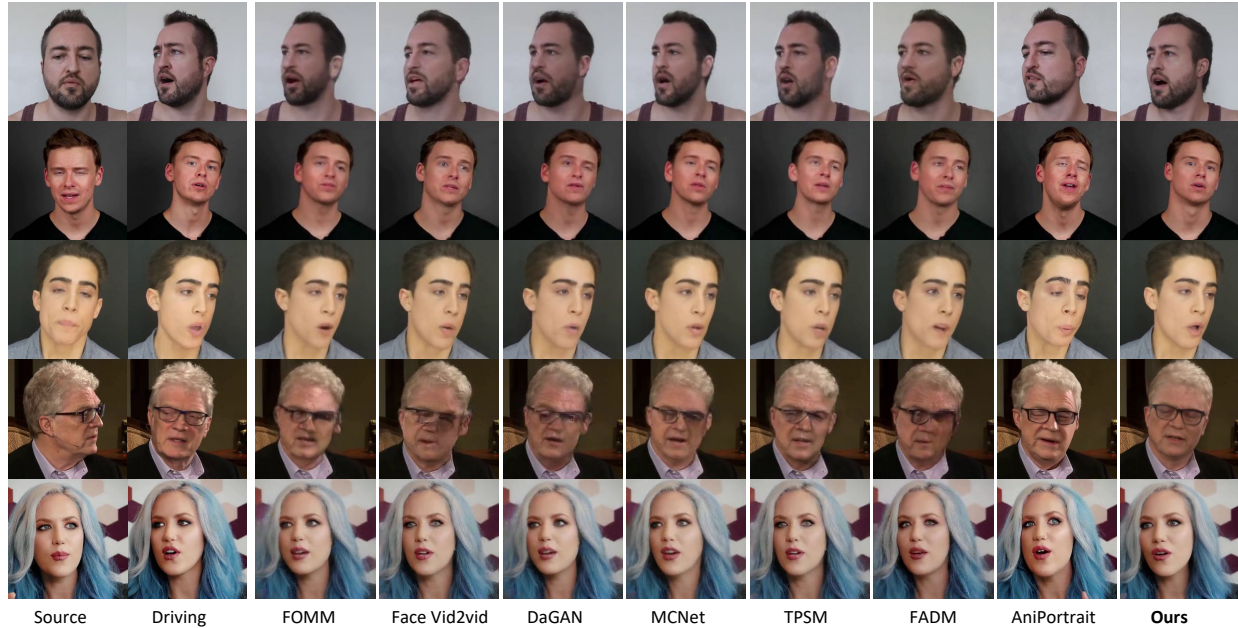


Figure 4. **Qualitative comparisons of self-reenactment.** The first four source-driving paired images are from TalkingHead-1KH [5] and the last ones are from VFHQ [51]. Our model faithfully preserves lip movements and eye gazes, handles large poses more stably, and maintains the identity of the source portrait better compared to other methods.

Distance (AED) [11], Average Pose Distance (APD) [11], and Mean Angular Error (MAE) of eyeball direction [16]. For self-reenactment, our models are evaluated on the official test split of the TalkingHead-1KH dataset [5] and VFHQ dataset [51], which consist of 35 and 50 videos respectively. For cross-reenactment, the first 50 images obtained from the FFHQ dataset [52] are used as source portraits. Detailed descriptions of these metrics are provided in Appendix A.

4.1. Self-reenactment

For each test video sequence, we use the first frame as the source input and animate it using the whole frames as driving images, which also serve as ground truth. For comparisons, the animated portraits and the ground truth images are down-sampled to a resolution of 256×256 to maintain consistency with the baselines. Qualitative and quantitative comparisons are detailed as follows.

Qualitative results. The qualitative comparisons are illustrated in Fig. 4. Our results are the pasted back images in the original image space using the first-stage base model. These cases demonstrate that our model can faithfully transfer motions from the driving images, including lip movements and eye gazes, while preserving the appearance details of the source portrait. The fourth case in Fig. 4 demonstrates that our model achieves stable animation results even with large poses, ensuring accurate transfer of poses.

Quantitative results. In Tab. 2, we present quantitative comparisons of self-reenactment. Our model slightly outperforms previous diffusion-based methods, such as FADM [9] and AniPortrait [12], in generation quality, and demonstrates better eyes motion accuracy than other methods.

4.2. Cross-reenactment

Qualitative results. Qualitative comparisons of cross-reenactment are shown in Fig. 5. The first two cases demonstrate our model’s ability to stably transfer motion under large poses from the driving or source portraits. The third and fourth cases show that our model accurately transfers delicate lip movements and eye gazes, maintaining appearance details consistent with the source portrait. Additionally, the last case illustrates that stitching enables our model to perform stably even when the face region in the reference image is relatively small, providing the capability to animate multi-person inputs or full-body images gracefully.

Quantitative results. Tab. 3 shows the quantitative results of the cross-reenactment comparisons. Our model outperforms previous diffusion-based and non-diffusion-based methods in both generation quality and motion accuracy, except for the FID on TalkingHead-1KH, where the FID of the diffusion-based method AniPortrait [12] is lower than ours. The flip side is that diffusion-based methods require much more inference time than non-diffusion-based methods due

Method	TalkingHead-1KH						VFHQ					
	PSNR \uparrow	SSIM \uparrow	LPIPS \downarrow	$\mathcal{L}_1\downarrow$	CSIM \uparrow	MAE ($^\circ$) \downarrow	PSNR \uparrow	SSIM \uparrow	LPIPS \downarrow	$\mathcal{L}_1\downarrow$	CSIM \uparrow	MAE ($^\circ$) \downarrow
FOMM [11]	31.0681	0.7620	0.1201	0.0419	0.8805	10.1745	30.5912	0.7098	0.1410	0.0505	0.8700	10.9327
Face Vid2vid [5, 43]	30.8438	0.7743	0.0940	0.0432	0.8774	10.8117	30.5166	0.7247	0.1132	0.0500	0.8775	11.1500
DaGAN [6]	31.3657	0.7903	0.0969	0.0389	0.8798	11.8655	30.7038	0.7315	0.1258	0.0481	0.8747	11.2051
MCNet [8]	<u>32.0013</u>	<u>0.8042</u>	0.1018	<u>0.0349</u>	<u>0.8876</u>	10.9035	<u>31.3459</u>	<u>0.7540</u>	0.1209	<u>0.0429</u>	0.8849	<u>9.6634</u>
TPSM [7]	31.2934	0.7965	0.0990	0.0395	0.8848	<u>9.6036</u>	31.0262	0.7476	0.1177	0.0466	<u>0.8884</u>	9.8169
FADM [9]	30.2141	0.7695	0.1049	0.0484	0.8708	11.4484	30.0932	0.7180	0.1252	0.0535	0.8707	11.7523
AniPortrait [12]	31.4669	0.7144	<u>0.0922</u>	0.0470	0.8550	12.0807	30.9013	0.6718	<u>0.1073</u>	0.0542	0.8570	14.2411
Ours	32.0082	0.8193	0.0664	0.0347	0.9125	7.0535	31.5616	0.7653	0.0798	0.0422	0.9121	6.6966

Table 2. Quantitative comparisons of self-reenactment.



Figure 5. **Qualitative comparisons of cross-reenactment.** The first three source portraits are from FFHQ [52] and the last two are celebrities. Driving portraits are random selected from TalkingHead-1KH [5], VFHQ [51] and NeRSemble [53]. We present the animated portraits without stitching in the cropping space, as well as the final results after stitching and pasting back into the original image space. Similar to self-reenactment, our model better transfers lip movements and eye gazes from another person, while maintaining the identity of the source portrait.

to multiple denoising steps and high FLOPs. Additionally, the temporal consistency of the foreground and background is not as good compared to non-diffusion-based methods, due to the high variability of the diffusion models. This phenomenon can be observed in Fig. 6, where self-reenactment cases from testsets of VFHQ and TalkingHead-1KH are exemplified. We also illustrate the results of MegActor [17] in Fig. 6, which is also a diffusion-based method sharing a similar mutual self-attention and plugged temporal attention architecture as AniPortrait [12] and AnimateAnyone [24].

4.3. Ablation Study and Analysis

In this section, we discuss the benefits and necessities of stitching, eyes and lip retargeting.

Ablation of the stitching module. As shown in the first block of Fig. 7, given a source image and a driving video sequence, the animated results without stitching share the same shoulder position as the driving frames. After stitching, the shoulder of the animated person is force aligned with the cropped source portrait while preserving the motion and appearance. In the second block of Fig. 7, after mapping into the original image space, it is clear that the animated portrait without stitching shows significant shoulder misalignment, while the stitched results show no visually apparent misalignment.

Ablation of eyes retargeting. In the first block of Fig. 8, the quantitative controllability of the eyes-open of the source image is illustrated. Without any driving motions, one can

Method	TalkingHead-1KH					VFHQ				
	FID↓	CSIM↑	AED↓	APD↓	MAE (°)↓	FID↓	CSIM↑	AED↓	APD↓	MAE (°)↓
FOMM [11]	90.8068	0.3057	0.7934	0.0411	18.3946	94.1640	0.2011	0.7374	0.0336	18.6282
Face Vid2vid [5, 43]	82.9066	0.3687	0.8285	0.0559	20.2687	83.8891	0.2360	0.7891	0.0470	19.9852
DaGAN [6]	81.1110	0.2937	0.7636	0.0405	21.0156	82.6255	0.1969	0.7108	0.0334	20.6918
MCNet [8]	89.3218	0.2863	<u>0.7163</u>	<u>0.0375</u>	<u>17.0721</u>	89.9694	0.1907	<u>0.6545</u>	0.0329	17.3642
TPSM [7]	80.5436	0.3289	0.7492	0.0387	17.4371	77.5867	0.2197	0.6700	<u>0.0290</u>	<u>16.8058</u>
FADM [9]	95.4043	<u>0.3755</u>	0.8158	0.0525	18.8346	98.2516	0.2473	0.7811	0.0438	18.9776
AniPortrait [12]	47.8739	0.3733	0.9127	0.0450	19.7136	<u>70.8077</u>	<u>0.2538</u>	0.9018	0.0501	20.1085
Ours	<u>58.0370</u>	0.3909	0.6772	0.0333	14.7946	56.4165	0.2606	0.6476	0.0271	13.3464

Table 3. Quantitative comparisons of cross-reenactment.

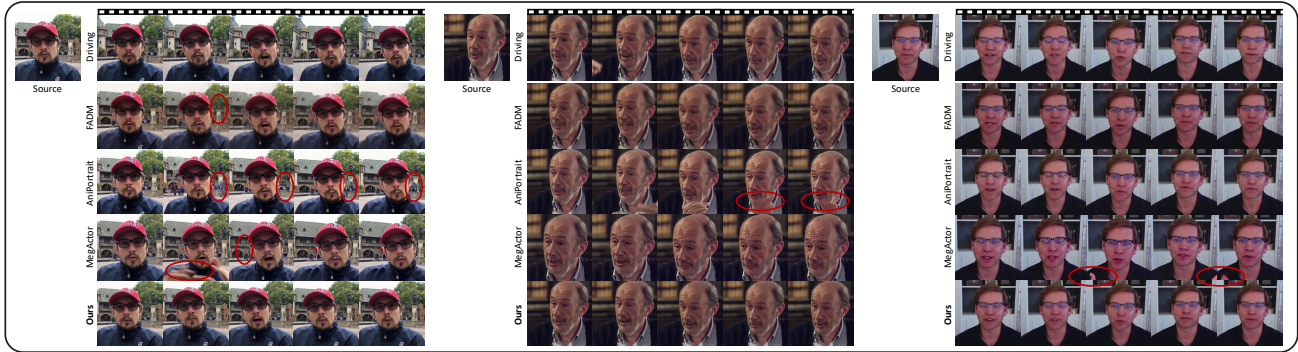


Figure 6. Temporal consistency comparisons with diffusion-based methods. These three cases are from VFHQ and TalkingHead-1KH test sets. Our animation results are in the original image space with stitching. Within the vertical circles, the statue disappears in the subsequent animated frames of FADM [9], there are pedestrian-like unnatural background movements in the animated results of AniPortrait [12], and the red banner disappears in some frames of MegActor [17]. Within the horizontal circles, there are hand-waving-like unnatural foreground movements in the animated images of both AniPortrait [12] and MegActor [17].

provide a proper driving eyes-open scalar $c_{d,eyes}$ from 0 to 0.8, send it to the eyes retargeting module \mathcal{R}_{eyes} along with the source eyes-open condition tuple $c_{s,eyes}$, and drive the eyes from closed to fully open. The eyes-open motion does not affect the remaining part of the reference image. Additionally, an out-of-training-distribution driving eyes-open scalar, such as -0.2 , can also achieve reasonable results. In the second block of Fig. 8, a cartoon image is animated by the driving frames of a closing-eye video. The eyes of the girl are much larger than those of the man in the first driving frame. Therefore, the driving eye-closing motion is too weak to close the girl’s eyes to the same extent, as observed in the second row without eyes retargeting. When we employed eyes retargeting, the driving eyes-open scalar $c_{d,eyes,i}$ corresponding to the i -th driving frame can be formulated as: $c_{d,eyes,i} = \bar{c}_{s,eyes} \cdot \frac{\bar{c}'_{s,eyes,i}}{\bar{c}'_{s,eyes,0}}$, where $\bar{c}'_{s,eyes,i}$ is the average value of the eyes-open condition tuple for the i -th driving frame, and the overline represents the averaging operation. Benefiting from eyes retargeting, the animated frames achieve the same eye-closing motion as the driving video.

Ablation of lip retargeting. Similarly, the first block of Fig. 9 illustrates the quantitative lip-open controllability of the source image. One can input a driving lip-open scalar $c_{d,lip}$ between 0 and 0.8, feed it to the lip retargeting module along with the source lip-open condition $c_{s,lip}$, and drive the lips from closed to fully open. The lip-open motion does not affect the remaining part of the source image. An out-of-training-distribution driving lip-open scalar can also achieve reasonable results, as depicted in Fig. 9. Additionally, the tongue is generated when the lips are widely open. As shown in the second block of Fig. 9, we can also drive the lip to close conditioned on a lip-close scalar $c_{d,lip,i}$ extracted from the driving frame: $c_{d,lip,i} = c_{s,lip} \cdot \frac{c'_{s,lip,i}}{c'_{s,lip,0}}$, where $c'_{s,lip,i}$ is the lip-open condition of the i -th driving frame.

Analysis on eyes and lip retargeting. A natural question is whether the eye and lip retargeting can take effect simultaneously, as described in Algorithm 1, when $\alpha_{eyes} = 1$ and $\alpha_{lip} = 1$. In other words, the core question is whether the retargeting modules have learned to distinguish the different patterns of Δ_{eyes} and Δ_{lip} . The two animation examples



Figure 7. **Ablation study of the stitching.** The first block shows the comparisons of stitching in the cropping image space, and the second block shows the comparisons after mapping into the original image space. The misalignment is apparent without stitching, especially in the shoulder region.

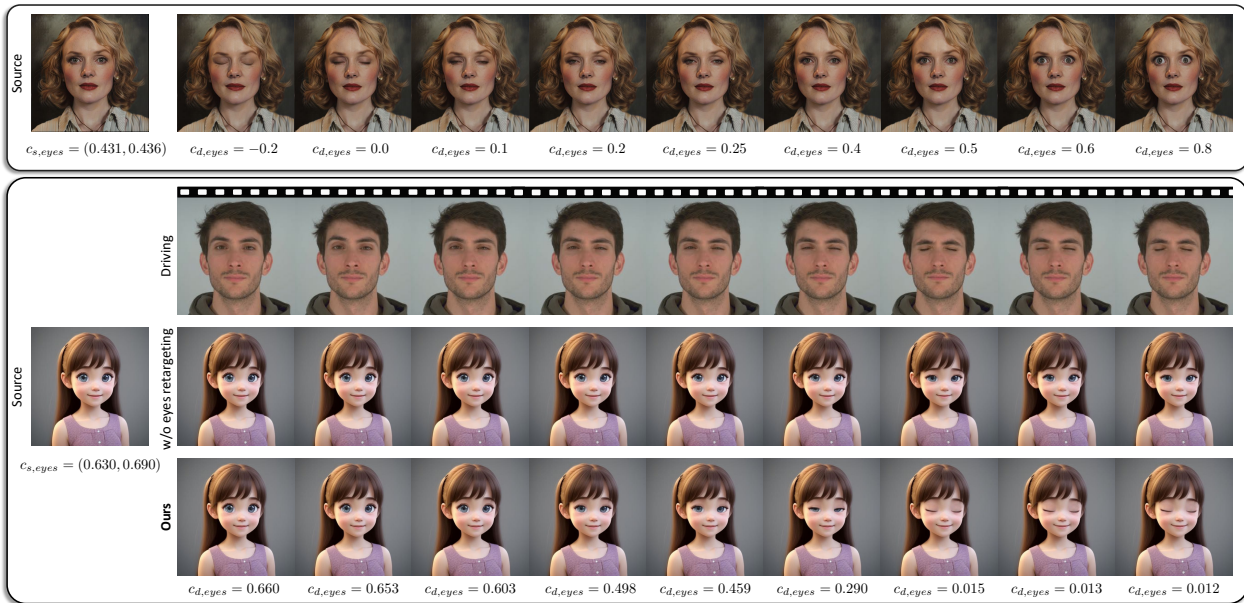


Figure 8. **Examples and ablation study of our eyes retargeting.** The first block shows the eyes-open controllability of our model on the source image without any driving frames. The second block demonstrates the ability of eye retargeting in cross-reenactment, especially when the eyes of the source person are much larger than the driving one. For clarity, the animated results adopt the source head rotation.

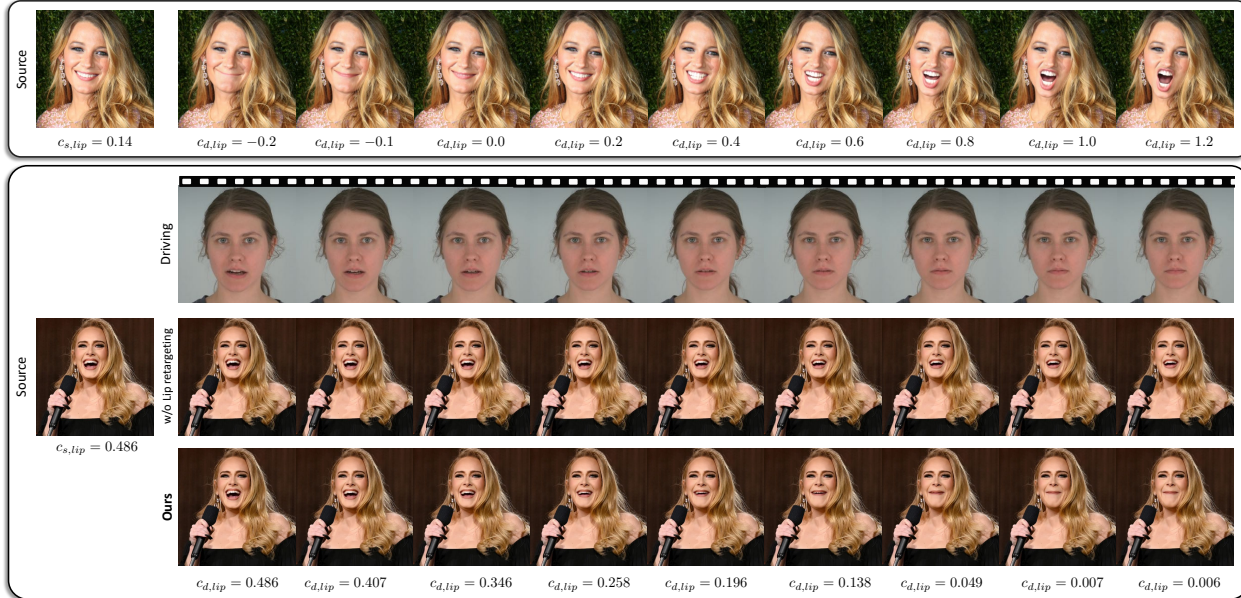


Figure 9. **Examples and ablation study of the lip retargeting.** Similar to eye retargeting, these two blocks show our controllability conditioned on arbitrary lip-open scalars, either randomly sampled or extracted from driving frames.



Figure 10. **Examples of simultaneous eyes and lip retargeting.** Given driving eyes-open and lip-open scalars simultaneously, the animated results from the source image suggest that eye and lip retargeting can be effective simultaneously, even though these two retargeting modules are trained independently.

in Fig. 10 positively support this hypothesis. The source images of the girls in ancient costumes can be animated to reasonable results with the given driving eyes-open and lip-open scalars, where Δ_{eyes} and Δ_{lip} are added to the driving keypoints simultaneously.

5. Conclusion

In this paper, we present an innovative video-driven framework for animating static portrait images, making them realistic and expressive while ensuring high inference efficiency and precise controllability. The generation speed of our model achieves 12.8ms on an RTX 4090 GPU using the naive Pytorch framework, while simultaneously outperforming other heavy diffusion-based methods. We hope

our promising results pave the way for real-time portrait animation applications in various scenarios, such as video conferencing, social media, and entertainment, as well as audio-driven character animations.

Limitations. Our current model struggles to perform well in cross-reenactment scenarios involving large pose variations. Additionally, when the driving video involves significant shoulder movements, there is a certain probability of resulting in jitter. We plan to address these limitations in future work.

Ethics considerations. Portrait animation technologies pose social risks, including misuse for deepfakes. To mitigate

these risks, ethical guidelines and responsible use practices are essential. Currently, the synthesized results exhibit some visual artifacts that could aid in detecting deepfakes.

Acknowledgments

We would like to thank our colleagues and partners Haotian Yang, Haoxian Zhang, Mingwu Zheng, Chongyang Ma, and others for their valuable discussions and insightful suggestions on this work.

References

- [1] Ian Goodfellow, Jean Pouget-Abadie, Mehdi Mirza, Bing Xu, David Warde-Farley, Sherjil Ozair, Aaron Courville, and Yoshua Bengio. Generative adversarial nets. In *NeurIPS*, 2014. 2
- [2] Robin Rombach, Andreas Blattmann, Dominik Lorenz, Patrick Esser, and Björn Ommer. High-resolution image synthesis with latent diffusion models. In *CVPR*, 2022. 2
- [3] Jonathan Ho, Ajay Jain, and Pieter Abbeel. Denoising diffusion probabilistic models. In *NeurIPS*, 2020.
- [4] Jiaming Song, Chenlin Meng, and Stefano Ermon. Denoising diffusion implicit models. In *ICLR*, 2020. 2
- [5] Ting-Chun Wang, Arun Mallya, and Ming-Yu Liu. One-shot free-view neural talking-head synthesis for video conferencing. In *CVPR*, 2021. 2, 3, 4, 6, 7, 8, 9
- [6] Fa-Ting Hong, Longhao Zhang, Li Shen, and Dan Xu. Depth-aware generative adversarial network for talking head video generation. In *CVPR*, 2022. 2, 3, 6, 8, 9
- [7] Jian Zhao and Hui Zhang. Thin-plate spline motion model for image animation. In *CVPR*, 2022. 2, 3, 6, 8, 9
- [8] Fa-Ting Hong and Dan Xu. Implicit identity representation conditioned memory compensation network for talking head video generation. In *ICCV*, 2023. 2, 3, 6, 8, 9
- [9] Bohan Zeng, Xuhui Liu, Sicheng Gao, Boyu Liu, Hong Li, Jianzhuang Liu, and Baochang Zhang. Face animation with an attribute-guided diffusion model. In *CVPR*, 2023. 2, 3, 6, 7, 8, 9
- [10] Arun Mallya, Ting-Chun Wang, and Ming-Yu Liu. Implicit warping for animation with image sets. In *NeurIPS*, 2022. 2, 3
- [11] Aliaksandr Siarohin, Stéphane Lathuilière, Sergey Tulyakov, Elisa Ricci, and Nicu Sebe. First order motion model for image animation. In *NeurIPS*, 2019. 2, 3, 6, 7, 8, 9
- [12] Huawei Wei, Zejun Yang, and Zhisheng Wang. Aniportrait: Audio-driven synthesis of photorealistic portrait animation. *arXiv preprint:2403.17694*, 2024. 2, 3, 6, 7, 8, 9
- [13] You Xie, Hongyi Xu, Guoxian Song, Chao Wang, Yichun Shi, and Linjie Luo. X-portrait: Expressive portrait animation with hierarchical motion attention. *arXiv preprint:2403.15931*, 2024. 2, 3
- [14] Yue Ma, Hongyu Liu, Hongfa Wang, Heng Pan, Yingqing He, Junkun Yuan, Ailing Zeng, Chengfei Cai, Heung-Yeung Shum, Wei Liu, and Qifeng Chen. Follow-your-emoji: Fine-controllable and expressive freestyle portrait animation. *arXiv preprint:2406.01900*, 2024. 2
- [15] Aliaksandr Siarohin, Oliver Woodford, Jian Ren, Menglei Chai, and Sergey Tulyakov. Motion representations for articulated animation. In *CVPR*, 2021. 2, 3
- [16] Yue Han, Junwei Zhu, Keke He, Xu Chen, Yanhao Ge, Wei Li, Xiangtai Li, Jiangning Zhang, Chengjie Wang, and Yong Liu. Face adapter for pre-trained diffusion models with fine-grained id and attribute control. *arXiv preprint:2405.12970*, 2024. 2, 3, 7
- [17] Shurong Yang, Huadong Li, Juhao Wu, Minhao Jing, Linze Li, Renhe Ji, Jiajun Liang, and Haoqiang Fan. Megactor: Harness the power of raw video for vivid portrait animation. *arXiv preprint:2405.20851*, 2024. 2, 3, 8, 9
- [18] Taras Khakhulin, Vanessa Sklyarova, Victor Lempitsky, and Egor Zakharov. Realistic one-shot mesh-based head avatars. In *ECCV*, 2022. 2
- [19] Ayush Tewari, Mohamed Elgharib, Gaurav Bharaj, Florian Bernard, Hans-Peter Seidel, Patrick Pérez, Michael Zollhofer, and Christian Theobalt. Stylerig: Rigging stylegan for 3d control over portrait images. In *CVPR*, 2020.
- [20] Partha Ghosh, Pravir Singh Gupta, Roy Uziel, Anurag Ranjan, Michael J Black, and Timo Bolkart. Gif: Generative interpretable faces. In *3DV*, 2020. 2
- [21] Volker Blanz and Thomas Vetter. A morphable model for the synthesis of 3d faces. In *SIGGRAPH*, 1999. 2
- [22] Nikita Drobyshev, Jenya Chelishev, Taras Khakhulin, Aleksei Ivakhnenko, Victor Lempitsky, and Egor Zakharov. Megaportraits: One-shot megapixel neural head avatars. In *ACM MM*, 2022. 2
- [23] Nikita Drobyshev, Antoni Bigata Casademunt, Konstantinos Vougioukas, Zoe Landgraf, Stavros Petridis, and Maja Pantic. Emoportraits: Emotion-enhanced multimodal one-shot head avatars. In *CVPR*, 2024. 2
- [24] Li Hu, Xin Gao, Peng Zhang, Ke Sun, Bang Zhang, and Liefeng Bo. Animate anyone: Consistent and controllable image-to-video synthesis for character animation. In *CVPR*, 2024. 2, 8
- [25] Di Chang, Yichun Shi, Quankai Gao, Jessica Fu, Hongyi Xu, Guoxian Song, Qing Yan, Yizhe Zhu, Xiao Yang, and Mohammad Soleymani. Magicpose: Realistic human poses and facial expressions retargeting with identity-aware diffusion. In *ICML*, 2024.
- [26] Zhongcong Xu, Jianfeng Zhang, Jun Hao Liew, Hanshu Yan, Jia-Wei Liu, Chenxu Zhang, Jiashi Feng, and Mike Zheng Shou. Magicanimate: Temporally consistent human image animation using diffusion model. In *CVPR*, 2024.
- [27] Johanna Karras, Aleksander Holynski, Ting-Chun Wang, and Ira Kemelmacher-Shlizerman. Dreampose: Fashion image-to-video synthesis via stable diffusion. In *ICCV*, 2023.
- [28] Tan Wang, Linjie Li, Kevin Lin, Yuanhao Zhai, Chung-Ching Lin, Zhengyuan Yang, Hanwang Zhang, Zicheng Liu, and Lijuan Wang. Disco: Disentangled control for realistic human dance generation. In *CVPR*, 2024. 2
- [29] Zipeng Qi, Xulong Zhang, Ning Cheng, Jing Xiao, and Jianzong Wang. Difftalker: Co-driven audio-image diffusion for talking faces via intermediate landmarks. *arXiv preprint:2309.07509*, 2023. 2

- [30] Shuai Shen, Wenliang Zhao, Zibin Meng, Wanhua Li, Zheng Zhu, Jie Zhou, and Jiwen Lu. DiffTalk: Crafting diffusion models for generalized audio-driven portraits animation. In *CVPR*, 2023.
- [31] Linrui Tian, Qi Wang, Bang Zhang, and Liefeng Bo. Emo: Emote portrait alive - generating expressive portrait videos with audio2video diffusion model under weak conditions. *arXiv preprint:2402.17485*, 2024.
- [32] Sicheng Xu, Guojun Chen, Yu-Xiao Guo, Jiaolong Yang, Chong Li, Zhenyu Zang, Yizhong Zhang, Xin Tong, and Baining Guo. Vasa-1: Lifelike audio-driven talking faces generated in real time. *arXiv preprint:2404.10667*, 2024.
- [33] Tao Liu, Feilong Chen, Shuai Fan, Chenpeng Du, Qi Chen, Xie Chen, and Kai Yu. Anitalker: Animate vivid and diverse talking faces through identity-decoupled facial motion encoding. *arXiv preprint:2405.03121*, 2024.
- [34] Cong Wang, Kuan Tian, Jun Zhang, Yonghang Guan, Feng Luo, Fei Shen, Zhiwei Jiang, Qing Gu, Xiao Han, and Wei Yang. V-express: Conditional dropout for progressive training of portrait video generation. *arXiv preprint:2406.02511*, 2024. 2
- [35] Arsha Nagrani, Joon Son Chung, and Andrew Senior. Voxceleb: a large-scale speaker identification dataset. In *Interspeech*, 2017. 3
- [36] Kaisiyuan Wang, Qianyi Wu, Linsen Song, Zhuoqian Yang, Wayne Wu, Chen Qian, Ran He, Yu Qiao, and Chen Change Loy. Mead: A large-scale audio-visual dataset for emotional talking-face generation. In *ECCV*, 2020. 3
- [37] Steven R Livingstone and Frank A Russo. The ryerson audio-visual database of emotional speech and song (ravdess): A dynamic, multimodal set of facial and vocal expressions in north american english. In *PLoS one*, 2018. 3
- [38] Mingcong Liu, Qiang Li, Zekui Qin, Guoxin Zhang, Pengfei Wan, and Wen Zheng. Blendgan: Implicitly gan blending for arbitrary stylized face generation. In *NeurIPS*, 2021. 3
- [39] Haotian Yang, Mingwu Zheng, Wanquan Feng, Haibin Huang, Yu-Kun Lai, Pengfei Wan, Zhongyuan Wang, and Chongyang Ma. Towards practical capture of high-fidelity relightable avatars. In *SIGGRAPH Asia*, 2023. 3
- [40] Haotian Yang, Mingwu Zheng, Chongyang Ma, Yu-Kun Lai, Pengfei Wan, and Haibin Huang. Vrm: A volumetric relightable morphable head model. *SIGGRAPH Asia*, 2024. 3
- [41] Kai Zhao, Kun Yuan, Ming Sun, Mading Li, and Xing Wen. Quality-aware pre-trained models for blind image quality assessment. In *CVPR*, 2023. 3
- [42] Sanghyun Woo, Shoubhik Debnath, Ronghang Hu, Xinlei Chen, Zhuang Liu, In So Kweon, and Saining Xie. Convnext v2: Co-designing and scaling convnets with masked autoencoders. In *CVPR*, 2023. 4
- [43] Longhao Zhao. Open face vid2vid. https://github.com/zhanglonghao1992/One-Shot_Free-View_Neural_Talking_Head_Synthesis, 2021. 4, 6, 8, 9
- [44] Taesung Park, Ming-Yu Liu, Ting-Chun Wang, and Jun-Yan Zhu. Semantic image synthesis with spatially-adaptive normalization. In *CVPR*, 2019. 4
- [45] Wenzhe Shi, Jose Caballero, Ferenc Huszár, Johannes Totz, Andrew P Aitken, Rob Bishop, Daniel Rueckert, and Zehan Wang. Real-time single image and video super-resolution using an efficient sub-pixel convolutional neural network. In *CVPR*, 2016. 4
- [46] Zhen-Hua Feng, Josef Kittler, Muhammad Awaiz, Patrik Huber, and Xiao-Jun Wu. Wing loss for robust facial landmark localisation with convolutional neural networks. In *CVPR*, 2018. 4
- [47] Jiankang Deng, Jia Guo, Xue Niannan, and Stefanos Zafeiriou. Arcface: Additive angular margin loss for deep face recognition. In *CVPR*, 2019. 5
- [48] Zhou Wang, Alan C Bovik, Hamid R Sheikh, and Eero P Simoncelli. Image quality assessment: From error visibility to structural similarity. In *TIP*, 2004. 6
- [49] Richard Zhang, Phillip Isola, Alexei A Efros, Eli Shechtman, and Oliver Wang. The unreasonable effectiveness of deep features as a perceptual metric. In *CVPR*, 2018. 6, 14
- [50] Martin Heusel, Hubert Ramsauer, Thomas Unterthiner, Bernhard Nessler, and Sepp Hochreiter. Gans trained by a two time-scale update rule converge to a local nash equilibrium. In *NeurIPS*, 2017. 6
- [51] Liangbin Xie, Xintao Wang, Honglun Zhang, Chao Dong, and Ying Shan. Vfhq: A high-quality dataset and benchmark for video face super-resolution. In *CVPR*, 2022. 7, 8
- [52] Tero Karras, Samuli Laine, and Timo Aila. A style-based generator architecture for generative adversarial networks. In *CVPR*, 2019. 7, 8
- [53] Tobias Kirschstein, Shenhan Qian, Simon Giebenhain, Tim Walter, and Matthias Nießner. Nersemble: Multi-view radiance field reconstruction of human heads. In *TOG*, 2023. 8
- [54] George Retsinas, Panagiotis P Filntisis, Radek Danecek, Victoria F Abrevaya, Anastasios Roussos, Timo Bolkart, and Petros Maragos. 3d facial expressions through analysis-by-neural-synthesis. In *CVPR*, 2024. 14
- [55] Ahmed A Abdelrahman, Thorsten Hempel, Aly Khalifa, Ayoub Al-Hamadi, and Laslo Dinges. L2cs-net: Fine-grained gaze estimation in unconstrained environments. In *ICFSP*, 2023. 14
- [56] Jiankang Deng, Jia Guo, Niannan Xue, and Stefanos Zafeiriou. Arcface: Additive angular margin loss for deep face recognition. In *CVPR*, 2019. 14
- [57] Tingchung Wan. Talkinghead-1kh-process. <https://github.com/tcwang0509/TalkingHead-1KH>, 2021. 14
- [58] Alec Radford, Jong Wook Kim, Tao Xu, Greg Brockman, Christine McLeavey, and Ilya Sutskever. Robust speech recognition via large-scale weak supervision. *arXiv preprint:2212.04356*, 2022. 14
- [59] Yingruo Fan, Zhaojiang Lin, Jun Saito, Wenping Wang, and Taku Komura. Faceformer: Speech-driven 3d facial animation with transformers. In *CVPR*, 2022. 14

A. Benchmark Metric Details

LPIPS. We use the AlexNet based perceptual similarity metric LPIPS [49] to measure the perceptual similarity between the animated and the driving images.

AED. AED is the mean \mathcal{L}_1 distance of the expression parameters between the animated and the driving images. These parameters, which include facial movement, eyelid, and jaw pose parameters, are extracted by the state-of-the-art 3D face reconstruction method SMIRK [54].

APD. APD is the mean \mathcal{L}_1 distance of the pose parameters between the animated and the driving images. The pose parameters are extracted by SMIRK [54].

MAE. To measure the eyeball direction error between the animated and the driving images, the mean angular error ($^\circ$) is adopted as: $\text{MAE}(I_p, I_d) = \arccos(\frac{\mathbf{b}_p \cdot \mathbf{b}_d}{\|\mathbf{b}_p\| \cdot \|\mathbf{b}_d\|})$, where \mathbf{b}_p and \mathbf{b}_d are the eyeball direction vectors of the animated image I_p and the driving image I_d respectively, and they are predicted by a pretrained eyeball direction network [55].

CSIM. CSIM measures the identity preservation between two images, through the cosine similarity of two embeddings from a pretrained face recognition network [56]. For self-reenactment, the CSIM is calculated between the animated and the driving images. For cross-reenactment, the CSIM is calculated between the animated and the source portraits.

FID. FID compares the distribution of animated images with the distribution of a set of real images. For TalkingHead-1KH test set, FID is calculated between the animated images and the last 38,400 images of the FFHQ dataset. For the VFHQ test set, FID is calculated between the animated images and the last 15,000 images of FFHQ.

Dataset processing. We follow [57] to pre-process the evaluation set of the TalkingHead-1KH. In cross-reenactment, we extract 1 frame every 10 frames from each video, for a total of 24 frames as the driving sequence. For VFHQ, we extract 1 frame every 5 frames, for a total of 6 frames.

B. Qualitative Results on Multi-person Portrait

We provide additional qualitative results on multi-person portrait animation in Fig. 13. Benefiting from the stitching ability of our model, each person in the portrait can be animated separately.



Figure 11. **Audio-driven examples.** This figure presents two examples of audio-driven portrait animation with stitching applied. The lip movements can be accurately driven by the audios input.

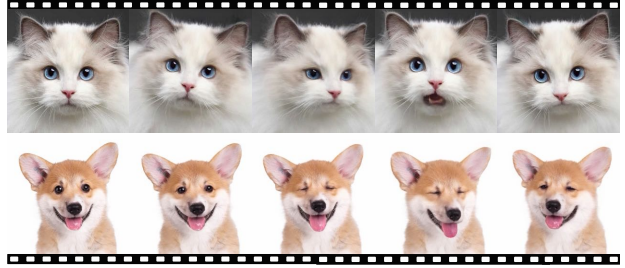


Figure 12. **Animal animation examples.** We show the animation results of a Ragdoll cat and a Corgi dog, with driving motions derived from human videos.

C. Audio-driven Portrait Animation

We can easily extend our video-driven model to audio-driven portrait animation by regressing or generating motions, including expression deformations and head poses, from audio inputs. For instance, we use Whisper [58] to encode audio into sequential features and adopt a transformer-based framework, following FaceFormer [59], to autoregress the motions. The audio-driven results are shown in Fig. 11.

D. Generalization to Animals

We find our model can generalize well to animals, *e.g.*, cats and dogs, by fine-tuning on a small dataset of animal portraits combined with the original data. Specifically, in the fine-tuning stage, we discard the head pose loss term \mathcal{L}_H , the lip GAN loss, and the faceid loss $\mathcal{L}_{\text{faceid}}$, as the head poses of animals are not as accurate as those of humans, the lip distribution differs from humans, and faceid cannot be applied to animals. Surprisingly, we can drive the animals with human driving videos, and the results are shown in Fig. 12.

E. Portrait Video Editing

We can extend our model to edit the head region of a source video sequence, while minimally sacrificing the temporal consistency of the source video. The source and driving



Figure 13. **Multi-person portrait animation examples.** Given a group photo of several subjects and a driving video sequence, our model can animate each subject with the stitching applied. The driving frame corresponding to each animated image is located in the left-down corner of the animated image.

implicit keypoints in Eqn. 7 are transformed as follows:

$$\begin{cases} x_{s,i} &= s_{s,i} \cdot (x_{c,s,i} R_{s,i} + \delta_{s,i}) + t_{s,i}, \\ x_{d,i} &= s_{s,i} \cdot \frac{s_{d,i}}{s_{d,0}} \cdot (x_{c,s,i} (R_{d,i} R_{d,0}^{-1} R_{s,i}) + \\ & (\delta_{s,i} + 0.5 \cdot (\delta_{d,i} + \delta_{d,i+1}) - \delta_{d,0})) + \\ & (t_{s,i} + t_{d,i} - t_{d,0}), \end{cases} \quad (8)$$

where $x_{s,i}$, $s_{s,i}$, $x_{c,s,i}$, $R_{s,i}$, $\delta_{s,i}$, $t_{s,i}$ represent the source keypoints, scale factor, canonical implicit keypoints, head pose, expression deformation, and translation of the i -th source frame, respectively. The operation $0.5 \cdot (\delta_{d,i} + \delta_{d,i+1})$ performs smoothing by averaging the expression offsets of the i -th and $(i + 1)$ -th driving frames. As exemplified in Fig. 14, the edited frame with stitching applied inherits the

expression from the corresponding driving frame, while preserving the non-head regions from the corresponding source frame.

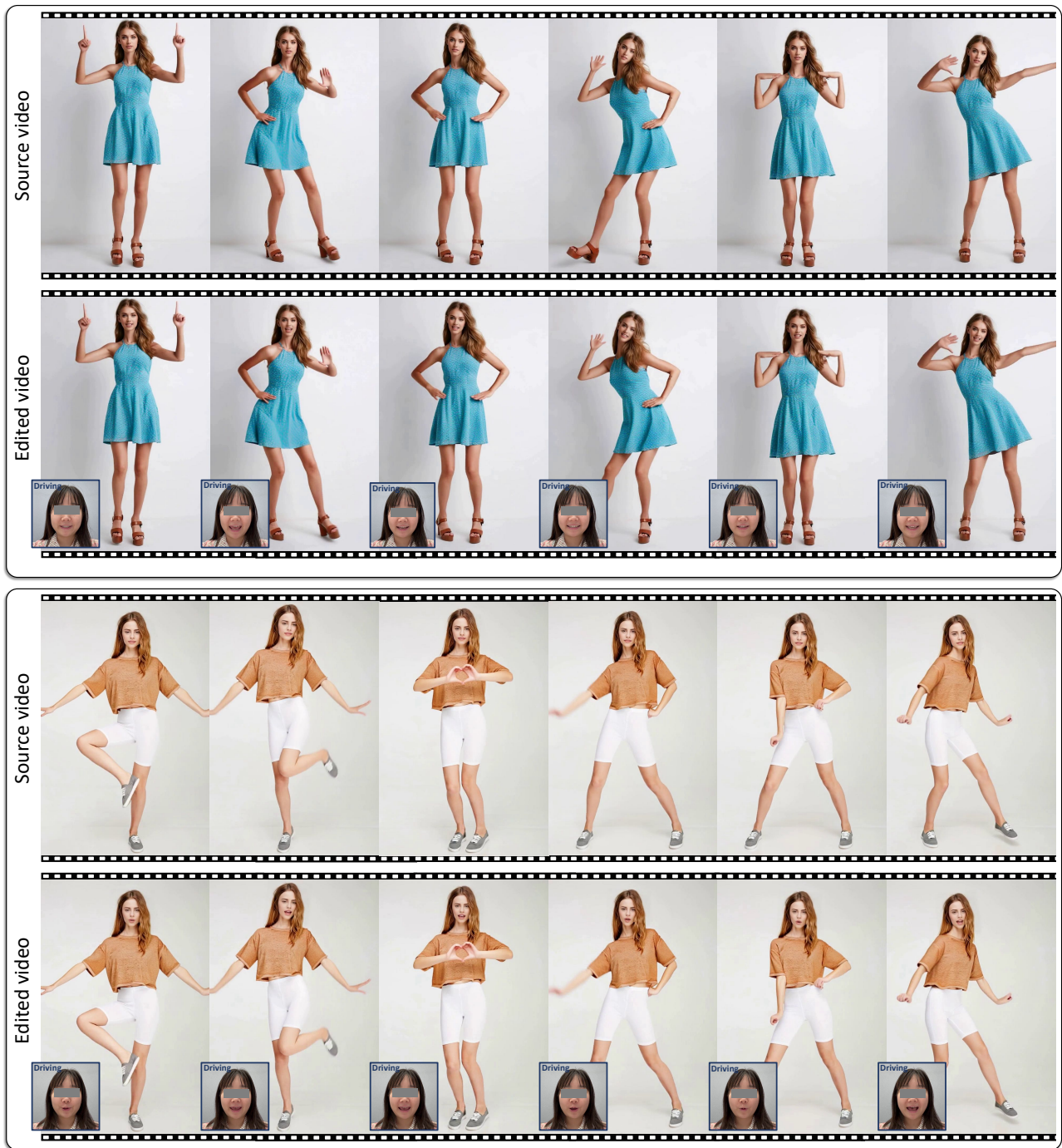


Figure 14. **Portrait video editing examples.** Given a source video sequence, such as a dancing video, our model can re-animate the head part using a driving video sequence. The edited video frame inherits the expression from the driving frame while preserving the non-head regions from the source frame.